From biological morphogenesis to engineering joint design: a bio-inspired algorithm

Kalenia Marquez-Florez, Santiago Arroyave-Tobón, Jean-Marc Linares

From biological morphogenesis to engineering joint design: a bio-inspired algorithm

Kalenia Marquez-Florez, Santiago Arroyave-Tobon, Jean-Marc Linares

Aix Marseille Univ, CNRS, ISM, Marseille, France

Abstract

Nature has developed smart strategies to morph joint contact surfaces as a response to local mechanical stimuli. Hence, it is compelling to explore the advantages of mimicking these strategies to design mechanical pieces. Researchers and engineers have developed generative design strategies mostly focused on structural topological and shape optimization. However, these generative strategies are not well developed for joint contact surfaces, even though they are critical points in engineering structures and machinery. This work presents a computational tool for adaptive surface shaping in contact problems inspired by the morphogenesis of synovial joints. The algorithm ~~behind~~ follows the cartilage growth rules, in which the hydrostatic and shear octahedral stresses either promote or inhibit an isotropic expansion of the local domain. The implementation is based on the finite element method and it is freely available on GitHub. A parametric study was performed to tune the parameters of the algorithm and it was successfully tested for two elastic bodies in unilateral contact. It was evidenced that the cartilage growth rules adapted the geometry of the surfaces in such a way that the contact stresses got uniformly distributed. This study is a step forward in the scope of bio-inspired generative designs.

Keywords: joint morphogenesis, bio-inspiration, elastic contact, surface shaping, DoE

1. Introduction

Nature has served as a mentor for the development of innovative designs due to its energy-efficient, adaptable and sustainable processes [1]. Synovial joints offer a good example of how nature transforms its structures in such a manner that they become durable, adaptable, and efficient enough, thereby vertebrates can accommodate easily in different ecological environments.

Synovial joints, when healthy, are relatively highly wear-resistant structures designed to provide a smooth relative movement between bones. The capacity of these structures to bear a lifetime of loading cycles is, in part, due to the unique characteristics of the tissues, but mainly, to their morphology which distributes efficiently stresses within it. **(author?)** [2] demonstrated that regardless of the complex geometry of the articular surfaces of a lamb elbow, the

Email address: kalenia-maria.marquez-florez@univ-amu.fr (Kalenia Marquez-Florez, Santiago Arroyave-Tobon, Jean-Marc Linares)

contact zones are located at the same radius, minimizing the kinematic heterogeneousness and therefore the energy loss [2]. Hence, it is compelling to apply synovial joint morphogenesis principles to the design of mechanical joints. In this way, load-adapted designs can be generated with an enhanced lifespan.

Researchers and designers have tried before to employ nature principles to design mechanical joints. This inspiration can either use the solution already given by nature (solution-based) or mimic the biological process that generates said solution (processes-based) [3].

Several works have taken solution-based approaches to address problems related to force and movement transmission. **(author?)** [4]. followed by **(author?)** [5]. identified several joint mechanisms found in nature and described their kinematics, actuators, and control. This inspired them to propose, first a two-degrees-of-freedom mechanism that resembles the structure and motion of the knee [4]. The authors proposed later a shape-changing flexible mechanism without sliding elements, therefore reducing energy dissipation and lubrication requirement [5]. **(author?)** [6] proposed a bushing bearing suited to misalignment, bio-inspired from a lamb elbow [6, 7]. They compared the wear performance of the obtained design against a classical bush bearing. The bio-inspired bearing showed lower pressures, an elliptic contact zone, and less wear rate than the classical one. Following this trend, **(author?)** [8] evaluated numerically and for different loading conditions, the load-bearing performance of bio-inspired designs based on the two morphologies that nature offers for one degree of freedom elbows, *i.e.* with and without a *trochlear sulcus* [8]. They found that the ones without *trochlear sulcus* had lower peak pressure values and larger contact areas, hence suitable for axial and combined loading; whereas the ones with *trochlear sulcus* were more suitable for bearing turnover moments [8].

However, the bio-inspiration to design mechanical joints can be focused at a further level of biomimesis: A processes-based approach. This, for instance, by adapting the strategies employed by nature to achieve their highly functional synovial joints (joint morphogenesis process) to the specific needs of the mechanical design.

Nature's strategy to develop synovial joints initiates with an uninterrupted condensation of mesenchymal cells (MSCs) within the developing limb, which later differentiate into chondrocytes (CCs) -cartilage cells, except at the site of the future joint (Interzone) (fig. 1) [9]. Then, the synovial capsule develops following the physical separation of the bone cartilaginous rudiments (cavitation). Joint morphogenesis takes place afterward regulated by a series of tissue adaptations that depends on biochemical and mechanical stimuli (fig. 1). However, it is mainly due to the proliferation of CCs that the cartilaginous bone rudiments grow and get their final shape [10, 11]. Simultaneously, the endochondral ossification is starting with the onset of the primary ossification center (POC), and subsequently, the onset of the secondary ossification center (SOC) [12]. These structures progressively ossify the cartilaginous bone rudiments until there only remains a layered cartilaginous structure between them, the growth plate.

Designers have proposed generative tools for the conception of contact pieces such as shape optimization (SO) or topological optimization (TO). These works have focused on obtaining a uniform contact pressure: SO by changing the shape of the bodies in contact [13, 14, 15, 16, 17, 18, 19, 20, 21], and TO by optimizing the material layout within a domain [22, 23, 24, 25]. Other designers have implemented frameworks that combine TO and SO to conceive

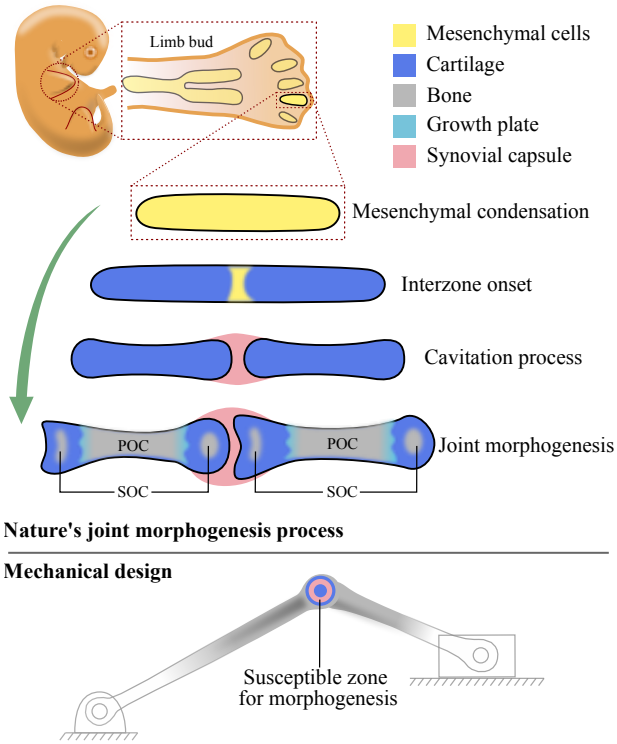

Figure 1: Representation of human upper limb development. Simplified scheme of the interphalangeal joint development process and the susceptible zones to bio-inspired morph in a mechanism. In nature, synovial joint development is marked by the onset of the Interzone within the condensation of mesenchymal cells in the limb bud. Subsequently, the physical separation of two cartilaginous bones takes place due to the cavitation process. Then, the joint morph thanks to the chondrocytes' response to mechanical and biochemical stimuli, which can promote either chondrocytes proliferation (growth and shaping) or chondrocytes hypertrophy (encouraging ossification, hence the onset of the POC and SOC). Within a mechanical design, the same principles on how the cartilage adapts to loading can be applied to morph a mechanical joint.

a two-component interlock, in which the contacting surfaces are modified as well as the material layout within the pieces [26]. However, these works only deal with the material distribution without modifying the shape of contact surfaces. **(author?)** [27] proposed a combined interface shape and material stiffness optimization method; in which both contact surfaces end up with the same geometry. Nevertheless, these methods (TO, SO, and **(author?)** [27]), do not seem to be potentially extrapolated for the design of mechanical pieces with relative movement between them (i.e. bushings and similar).

To date, only the authors' research group has made an initial approach to the application of the synovial joint morphogenesis principles to design mechanical pieces, demonstrating the feasibility of applying the cartilage growth laws in the automatic design of contact surfaces [28]. However, the way of establishing the process parameters and their influence on the final shape is not discussed. Apart from this previous work, the authors have not found other evidence in the literature in which joint morphogenesis has been applied to propose novel mechanical joint designs.

Hence, this work proposes a computational implementation of a bio-inspired algorithm for contact surface shaping and a parametric study followed by an optimization of these parameters. The algorithm is based on the biological principles of joint morphogenesis (section 2). The case of two elastic bodies in unilateral contact under static con-

ditions is studied (section 3.1). The biological joint morphogenesis process was translated to a mechanical setting (section 3.2). The problem was formulated following a normalized approach (section 3.3) so that it could be solved independently of the applied force and the dimensions of the initial geometry. Buckingham's Pi Theorem was used to define the minimal set of dimensionless parameters that govern the bio-inspired process (section 3.4). The algorithm was implemented using the finite element method (section 3.5). The most influential parameters of the algorithm were optimized following a design of experiments (DoE) strategy (section 3.6). Using the optimized algorithm, a contact profile was obtained in a generative way, mimicking the cartilage growth (section 4). Due to the stress-dependent nature of the process, the obtained contact profile is well adapted to the applied load. This study is a stepping stone for the development of a generative design framework inspired by nature's joint morphogenesis process. Additionally, it can also draw some conclusions on how to develop more efficient mechanical pieces, and give some insights into how nature adapts itself to the mechanical environment.

2. On joint onset and morphogenesis

This section carries out a literature review of the joint onset and morphogenesis processes is carried out. Also, an exploration of computational models found in the literature that aimed to explain joint development-related processes is performed. These models are the base of the morphogenesis-inspired process for designing contact profiles developed in this work. Finally, some conclusions that condensate the theories and computational models are portrayed.

2.1. Overview of joint onset and morphogenesis

The development of synovial joints initiates with an uninterrupted condensation of MSCs (skeletal blastema) within the early limb bud. These MSCs then differentiate into CCs, however, on the site of the future joint the CCs will de-differentiate to MSC; this place is known as the Interzone and is formed by packed layered condensation of MSCs [29]. This first step of joint development is known as Interzone onset [30].

The definitive separation of the future bones (at this moment still cartilaginous), occurs with the cavitation process. At this stage, a cavity is created between the cartilaginous molds which will be filled by synovial fluid. The cleavage is due to the differentiation of the MSCs within the Interzone into other joint tissues (capsule, meniscus, ligaments, etc.) [31], or even apoptosis (programmed cell death) [31, 32, 33]. The cartilaginous bones acquire their initial shape during the Interzone onset and the cavitation process, either by CCs proliferation or due to the shape of the Interzone [34, 35].

2.2. Chondrocyte mechanical response

In parallel, the muscles are developing from the base of the limb bud, and as they form the growing limbs increase their movement, twitching, stretching, etc. [36]; in fact, studies have shown that the mechanical effects due to these movements are necessary for a normal joint formation [37]. Thus, being the bones still in their cartilaginous state,

the joint morphing process is highly dependent on the response of the CCs to mechanical stimuli, mainly on their proliferation, hypertrophy, and matrix production rates.

Carter and associates have proposed a theory of growth and ossification during the development of synovial joints (known as Carter's theory) [38, 39, 40, 41, 42, 11]; in essence, they suggest that intermittent octahedral shear stress accelerates chondrocyte hypertrophy (and subsequent ossification of the tissue), whereas cyclic compressive hydrostatic stress maintains cartilage in its current state, *i.e.* proliferative, which translates into growth of cartilaginous tissue. This theory has been complemented by other experimental studies [43, 44, 45, 46, 47].

2.3. Biochemical factors

Undoubtedly, not only do mechanical stimuli affect joint morphogenesis but also biochemical factors. The biochemical system between the Parathyroid Hormone-related Protein (PTHrP) and the Indian Hedgehog (Ihh) has relatively high importance in the development of long bones [48]. Ihh is said to control CCs proliferation, maturation, and hypertrophy [49]. PTHrP inhibits CCs hypertrophy, keeping them in a proliferative state [50]. The key point in the PTHrP-Ihh system is that these molecules have a negative autoregulatory loop, which leads to a concentration gradient that defines the proliferative zone size and rate. It should be recalled that it is the proliferation of the CCs that regulates the growth of the cartilaginous tissue. PTHrP is highly concentrated at the periarticular perichondrium (where the articular cartilage will be) of cartilaginous bones and diffuses to the growth plate. Then, where the concentration of PTHrP drops below a critical threshold, the proliferation of CCs stops and they start to hypertrophy [48]. Ihh is expressed by these early hypertrophic cells, which stimulates the synthesis of PTHrP.

2.4. Cartilage growth mathematical models

Computational models have been developed to simulate joint morphogenesis, in which the growth of the tissue is regulated by the proliferation of the CCs and proportional to the CCs population density and the hydrostatic stress [51, 52, 10].

The first model was developed by **(author?)** [51], who followed the Hueter-Volkmann law; the latter argues that growth is reduced by an increased compression loading [53]. They modeled growth through a tensor $\mathbf{G} = \lambda\mathbf{I}$, where λ is a scalar measure of the growth and $\mathbf{I}$ is the identity tensor [51]. The scalar term $\lambda = k_b\psi_b + k_m\psi_m$ was a linear combination of a mechanobiological stimulus ψ_m (which depended on the stress history) and a biological growth stimulus ψ_b (function of the position along the long axis of the bone rudiment), where k_b and k_m are the relative strength of the biological and mechanobiological stimuli. They obtained relatively congruent surfaces, however, it must be considered that the Hueter-Volkmann law is a qualitative law that does not take into account the load history and is mainly proposed for growth plates and bone growth [53].

Several years later, **(author?)** [52] proposed a model in which implemented a growth rate: $\dot{\varepsilon} = \dot{\varepsilon}_b + \dot{\varepsilon}_m$, where $\dot{\varepsilon}_b$ is the biological contribution to growth (considered in a similar manner that in **(author?)** [51]) and $\dot{\varepsilon}_m$, the mechanical contribution to growth, was proportional to the compressive hydrostatic stress [52]. They modeled growth as a thermal

isotropic expansion in which $\dot{\varepsilon}$ was used as 'temperature'. Additionally, they included a synovial capsule and evaluated its effect on the joint morphogenesis process. They also obtained relatively more congruent shapes of the two joining bones compared to the previous model.

Following **(author?)** [52], **(author?)** [10]. developed a computational model for the morphogenesis of an interphalangeal joint. They considered a molecular pattern (PTHrP-Ihh) which dictated what zones of the cartilaginous rudiments were proliferative (allowed to grow) [10]. As in **(author?)** [52], they also included an incompressible synovial capsule. Regarding the mechanical growth rules, they considered that cyclic hydrostatic compressive stress promoted growth; however, if the octahedral shear stress was above a threshold, the growth was inhibited (Carter's law). In that work, growth was modeled as an imposed strain: $\mathbf{d} = \alpha C co^{-1} S_{\mathrm{hyd}} \mathbf{I}$, which depended on a constant cellular concentration Cco and the compressive hydrostatic stress S_{hyd}. They obtained a congruent joint similar to an interphalangeal joint.

2.5. Literature review conclusions

Some conclusions might be drawn from the aforementioned models and the reviewed literature: (1) a biochemical gradient function along the long axis of the rudiments is necessary to determine the proliferative zones that will add to the overall growth of the bone; (2) compressive cyclic hydrostatic stress promotes growth; (3) high octahedral shear stress inhibits cellular proliferation, hence growth; (4) the synovial capsule has an important role in the joint morphogenesis. From these conclusions, a simplified biological process is proposed (fig. 2).

3. Materials and methods

The bio-inspired process was implemented using normalized variables to solve the problem independently of the applied force and the dimensions of the initial geometry. The minimal set of dimensionless parameters governing the bio-inspired process was identified by applying Buckingham's Pi theorem. This set of parameters was optimized by following a DoE strategy. Two contact profiles were obtained generatively (mimicking cartilage growth) using the algorithm with the optimized parameters. The implementation and optimization of the algorithm are explained in the next sections. The implementation is based on the finite element method and it is freely available on GitHub[1].

3.1. Unilateral contact problem

This study aims to morph the contact surface of two elastic bodies, one upper body, and one lower body, by following nature's rules of growth (fig. 3). The contact surface of the upper body starts as a hemispheric geometry of constant radius ($R_u = const$), *i.e.* the local radius is constant regardless the point on the surface; for the lower body, the contact surface starts as a semi-infinite half-space ($R_l = \infty$) (fig. 3 -left). An external distributed static force $\mathbf{F}$ is applied on the top of the upper body. Both bodies have the same material properties (E and ν). The upper body is

[1] `https://github.com/sarroyavet/BioDesign_joint_morphogenesis`

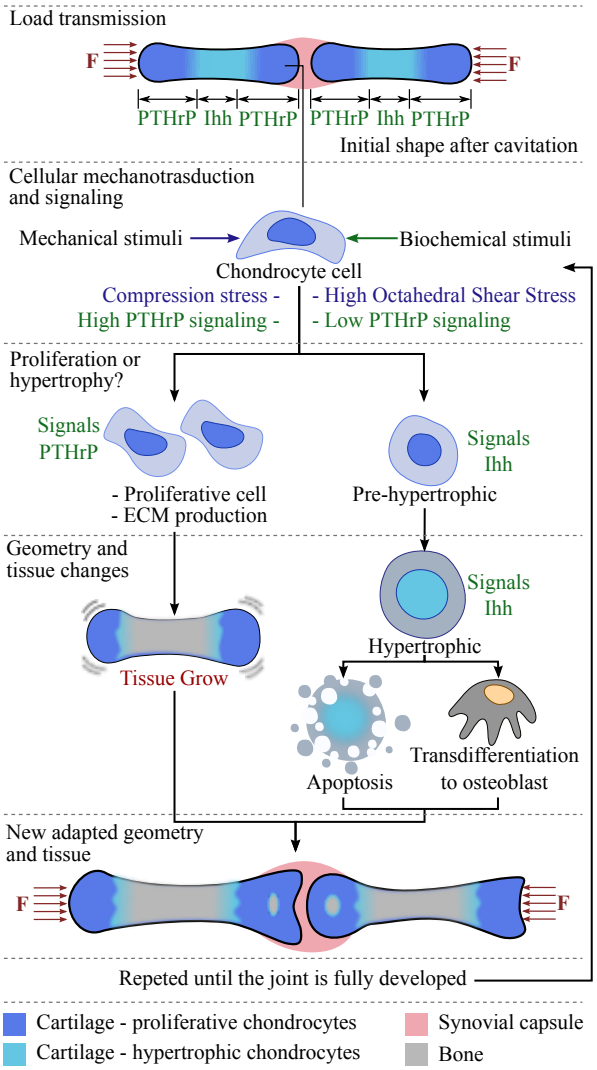

Figure 2: Chondrocyte cells adaptation rules. The cartilaginous bone rudiments are subjected to mechanical loading and, within it, an autoregulatory loop of Ihh-PTHrP. The CCs react to the mechanical and biochemical stimuli, depending on which these CCs can either proliferate or become hypertrophic. If the cell proliferates, means that the tissue (cartilage) must grow and morph; but if the cell becomes hypertrophic, then the tissue ossifies. This process continues until a full-grown ossified bone is achieved.

allowed to move along its vertical axis; the bottom boundary of the lower body can only move in the horizontal plane, except for the central point, which is fixed.

A bio-inspired morphogenesis process is then applied to both bodies (fig. 3 -center). The process promotes growing (or expansion) at certain zones, allowing the parts to adapt to the mechanical loading. A couple of adapted surfaces are obtained at the end of the process; the contact profiles depend on the x coordinate (fig. 3 -right), *i.e.* $R_u = f(x)$ for the upper body, and $R_l = g(x)$ for the lower body.

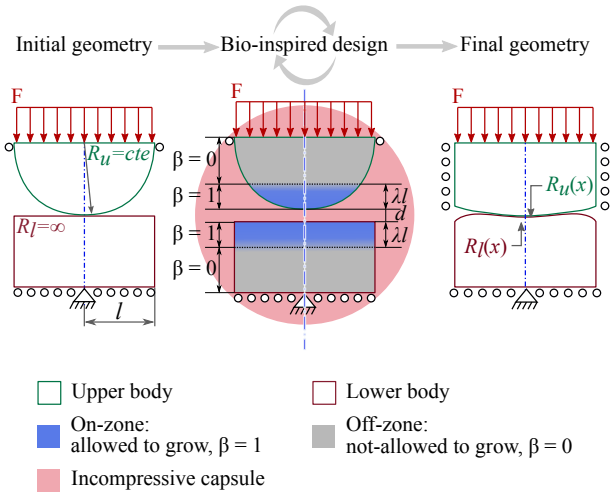

Figure 3: Application of the bio-inspired process for contact surface morphogenesis to a generic contact problem with elastic bodies and a static load (**F**). Left: A hemispheric geometry of constant radius $R_u = const$(upper body, green contour) and a semi-infinite half-space (lower body, red contour) in contact subjected to the joint morphogenesis process. Center: The pieces act as bone rudiments, and a capsule is included (pink region). The blue zone represents a bio-molecular gradient that acts as an on/off switch for growth. Right: Morphed contact surfaces; the upper and lower body shapes its contact profile depending on the x coordinate ($R_u = f(x)$ & $R_l = g(x)$).

3.2. *From biological joint morphogenesis to mechanical design*

Following the biological process described in section 2, one similar is proposed to emulate morphogenesis in mechanical pieces. The concepts considered within the bio-inspired process and its biological equivalent are presented in table 1 and are explained hereafter.

Mimicking the biological process, the mechanical pieces (equivalent to cartilaginous bone rudiments) are embedded in a structure that resembles the synovial capsule, *i.e.*, a spherical incompressible domain with material properties E_c and ν_c (fig. 3-center) (as done in **(author?)** [52, 10]).

Additionally, as in all biological joint morphogenesis models, there is a bio-molecular gradient involved, which can either add to the growth [51, 52] or act as an on/off switch for growth [10]. For the bio-inspired process, a switch was included through the *growth potential* (β), hence, $\beta = 1$ (blue zones within the bodies, fig. 3-center) when the zone is allowed to grow, and $\beta = 0$ when not (grey zones within the bodies, fig. 3-center). A smooth transition from the on-zone to the off-zone was implemented. Notice in fig. 3 that the zone allowed to grow is the one closer to the zone of interest, *i.e.*, the contacting surfaces. The length of these 'epiphyses', or zone allowed to grow, was defined as proportional to the initial width of the pieces through the *'epiphyses' length factor*, λ (fig. 3-center).

In the biological process, hydrostatic compressive stress promotes the proliferation of chondrocytes [51, 52, 10], so tissue growth; therefore, within the bio-inspired process, the pieces will 'grow' proportionally to this same compression hydrostatic stress (σ_{hyd}). In nature the octahedral shear stress (τ_{oct}), when high enough, inhibits the proliferation of chondrocytes, hence preventing growth. Within the bio-inspired process, the von Mises' stress (σ_{vm}), which is an engineering equivalent proportional to τ_{oct}, was taken to inhibit the growth of the local domain: If σ_{vm} is above a threshold (σ_{lim}), the local domain cannot grow. From this, a *growth factor* (G_f) can be defined, which acts as a local

Table 1: From nature to mechanical design. Concepts equivalencies between the synovial joint morphogenesis process and the bio-inspired mechanical joint design process

Synovial joint morphogenesis	**Bio-inspired joint design**
Cartilaginous bone rudiments: Cartilaginous structures go through morphogenesis and endochondral ossification, and eventually, become long bones.	*Mechanical pieces*: Within the bio-inspired process, these pieces go through morphogenesis to give rise to an adapted contact surface profile.
Synovial capsule: Completely close structure filled with synovial fluid that surrounds the synovial joint.	*Incompressible capsule*: A spherical incompressible domain surrounding the pieces, that allows a uniform loading transmission between them while vouching for the continuity of the domain.
Molecular pattern: Biochemical distribution within the bone rudiments, that determines cellular behaviors (biochemical stimuli). The PTHrP-Ihh system is the one that most influences the development of long bones. This signaling can be influenced by other bio-molecular or mechanical stimuli.	*Growth potential* β: Variable which acts as an on/off switch, and defines the zones of the pieces domain that are susceptible to growth through the morphogenesis process.
Growth factors: Molecules produced by cells to signal (communicate) to their neighbor peers the stimuli, biochemical or mechanical, they are sensing. These signals trigger a chain of events; cells can amplify the signal or initiate processes (*i.e.* cell proliferation).	*Growth factor* G_f: Variable that indicates the amount of growth in function of the mechanical stimuli (σ_{hyd}, σ_{vm}, & σ_{lim}) and the growth potential (β).
Cellular proliferation rate: Tissue growth during joint morphogenesis is mainly due to cell proliferation; it is the proliferation rate and the direction of the cell division that influences the tissue proportions. This proliferation rate is defined by the maturation of the cell and, in the case of the chondrocytes, their level of hypertrophy.	*Growth coefficient* α: Parameter that indicates the rate at which the local domain expands with an increase of G_f. As in nature, this coefficient is set to evolve from a high value to a small one, to account for the 'maturation' of the domain of the mechanical pieces, *i.e.*, the domain growth coefficient diminishes at each growth step (g_s). The latter allows a large growth at the beginning and fine geometric adjustments at the end.
Tissue growth: As mentioned before, the morphogenesis of the bone rudiments is mainly due to cellular proliferation, without changing the cellular density within the tissue.	*Piece growth*: The pieces growth is due to a volumetric change proportional to the mechanical conditions.

signaling value for how the local domain will grow. G_f depends on β, σ_{hyd}, σ_{vm} and σ_{lim} (see eq. (1)).

$$G_f = \begin{cases} \beta|\sigma_{\text{hyd}}| & \text{if } \sigma_{\text{hyd}} \leq 0 \ \& \ \sigma_{\text{vm}} < \sigma_{\text{lim}}, \\ 0 & \text{for other cases} \end{cases} \tag{1}$$

In nature, joints morph gradually until the SOC ossifies the entire epiphyses. Therefore, in the bio-inspired process, the parameter *growth coefficient* (α) was defined. The growth coefficient, indirectly, involves the 'maturation' and 'ossification' of the domain, hence, it should evolve from a high value, α_0, to null in several given stages (steps). Seen from a biological point of view, a high value of α means that the chondrocytes are highly proliferative whereas a low α, indicates low proliferative cells (hypertrophic) and that most of the tissue has ossified. This parameter allows having large growth rates (adaptations) at the beginning of the process and small adjustments by the end.

Growth can be simulated as a local volumetric expansion of the domain proportional to the G_f and α. The local change of volume ($\Delta V/V$) can be expressed as follows (eq. (2)):

$$\frac{\Delta V}{V} = \alpha G_f \tag{2}$$

The structure of eq. (2) resembles the one of mechanical thermal expansion; being α the coefficient of thermal expansion and G_f the temperature change. As α depends on the number of growth steps g_s, *i.e.* $\alpha_i = s(i)$, where i is the current growth step (goes from 0 to g_s), the area under the curve $s(i)$ can be seen as the total rate of change volume used for growth. Then, it is possible to have the same outcome with two different functions of $s(i)$ as long as the integrals of the functions are the same.

3.3. Stress normalization

The stresses were normalized to make the morphogenesis process independent of the applied force **F** and the initial dimension of the pieces. Then, at each growth step both analyzed stresses, σ_{hyd} and σ_{vm}, get normalized by the maximum of each within the domain:

$$\bar{\sigma}_{\text{hyd}} = \sigma_{\text{hyd}} \left(\sigma_{\text{hyd}}^{\text{max}}\right)^{-1} \tag{3}$$

$$\bar{\sigma}_{\text{vm}} = \sigma_{\text{vm}} \left(\sigma_{\text{vm}}^{\text{max}}\right)^{-1} \tag{4}$$

where $\bar{\sigma}_{\text{hyd}}$ and $\bar{\sigma}_{\text{vm}}$ are the normalized hydrostatic stress and von Mises' stress, respectively; σ_{hyd} and σ_{vm} are the local hydrostatic and von Mises' stresses; and $\sigma_{\text{hyd}}^{\text{max}}$ and $\sigma_{\text{vm}}^{\text{max}}$ are the maximum hydrostatic and von Mises' stresses within both the pieces in contact.

Table 2: Parameters the bio-inspired process.

no	*parameter name*	*letter*
-	External load	F
-	Radius of the upper piece	$R_s(l)$
-	Radius of the lower piece	$R_l(l)$
1	Pieces Poisson's ratio	ν
2	Capsule Poisson's ratio	ν_c
3	Capsule thickness	d
4	Pieces Width	l
5	'Epiphyses' length factor	λ
6	von Mises' Stress limit	σ_{lim}
7	Capsule Young's modulus	E_c
8	Pieces Young's modulus	E
9	Initial growth coefficient	α_0

3.4. Dimensionless analysis

Buckingham's Pi Theorem was used to define a minimal set of dimensionless parameters that govern the bio-inspired process. The set of parameters for the bio-inspired process is listed in table 2. The magnitude of the external load and the initial dimension of the pieces were not considered as the stresses are normalized (section 3.3). According to Buckingham's pi-theorem, the problem can be reduced from 9 to 7 dimensionless parameters. The chosen set of

dimensionless parameters is shown table 3. Notice that α has the inverse units G_f (see eq. (2)), however, since the stresses are normalized, α is also dimensionless.

Table 3: Dimensionless parameters for the bio-inspired process.

no	*parameter name*	*letter*	
1	Bodies Poisson's ratio	ν	
2	Capsule Poisson's ratio	ν_c	
3	Capsule thickness factor	$\bar{d}$	$= d/l$
4	'Epiphyses' length factor	λ	
5	Normalized von Mises' Stress limit	$\bar{\sigma}_{\text{lim}}$	
6	Young's ratio	θ	$= E/E_c$
7	Initial growth coefficient	α_0	

3.5. Bio-inspired algorithm for contact surface morphogenesis

A bio-inspired algorithm for contact surface morphogenesis was proposed based on the equivalent biological process (see algorithm 1). This algorithm considers the mechanical equivalents of biological concepts, the normalization, and the dimensionless analysis explained in the previous sections. It was implemented in a computational framework based on the finite element method (FEM). For the implementation, the finite element analysis (FEA) software tool *EDF Code_Aster* was employed.

The algorithm has as input the magnitude of the loading $F = 100\text{N/mm}^2$ and the material properties of the pieces, $E = 100\text{GPa}$ and $\nu = 0.3$. The rest of parameters: The ones related to initial geometry, $l = 5\text{mm}$, $R_u = l$, and $R_l = \infty$; and those of the bio-inspired process are treated in section 3.6.

Then, some variables required for the process are initialized (line 1 - line 4). Once every parameter is defined, a recursive subroutine can start, which depends on the value of α (line 5 - line 34). Within the **while** loop (line 5), some geometrical tasks are performed; first, the mesh of the upper body, A_1 (line 6), and lower body A_2 (line 7), are created and located in such a way that the smallest distance between their contact surfaces is d. Then, the geometry and mesh of the capsule, A_3, is generated (large enough to contain completely both meshes A_1 and A_2) (line 8).

Algorithm 1 Bio-inspired process algorithm

Require: F, E, ν
Ensure: $l, R_l(l), R_u(l)$
1: Define $\nu_c, \theta, \bar{\sigma}_{\text{lim}}, \lambda, \alpha_0, \bar{d}$
2: $E_c \leftarrow E/\theta$
3: $\alpha \leftarrow \alpha_0$
4: $i \leftarrow 0$ ▷ Step counter
5: **while** $\alpha > 0$ **do**
6: Create the mesh of the upper body: A_1
7: Create the mesh of the lower body: A_2
8: Create the mesh of the capsule: A_3
9: Assign to A_1 and A_2: E, ν
10: Assign to A_3: E_c, ν_c
11: Apply F and boundary conditions
12: Get σ_{hyd} & σ_{vm} from FEA mechanical
13: $\sigma_{\text{hyd}}^{\max} \leftarrow max(\sigma_{\text{hyd}})$ in A_1 & A_2
14: $\sigma_{\text{vm}}^{\max} \leftarrow max(\sigma_{\text{vm}})$ in A_1 & A_2
15: **for** each element j in $A_{1,2}$ **do**
16: $\bar{\sigma}_{hyd_j} \leftarrow \sigma hyd_j \left(\sigma_{\text{hyd}}^{\max}\right)^{-1}$
17: $\bar{\sigma}_{vm_j} \leftarrow \sigma vm_j \left(\sigma_{\text{vm}}^{\max}\right)^{-1}$
18: $\beta_j \leftarrow 0$ ▷ Initialize growth potential
19: $G_{f_j} \leftarrow 0$ ▷ Initialize growth factor
20: **if** $\bar{\sigma}_{vm_j} \leq \sigma lim$ **then**
21: **if** $\bar{\sigma}_{hyd_j} \leq 0$ **then**
22: $\beta_j \leftarrow 1$, if $0 \leq y_j \leq \lambda l$
23: $G_{f_j} \leftarrow \beta_j \left|\bar{\sigma}_{hyd_j}\right|$
24: **end if**
25: **end if**
26: **end for**
27: Use $\mathbf{G_f}$ as temperature
28: Use α as expansion coefficient
29: Get $\Delta V/V$ from a FEA thermal
30: Deform the A_1 & A_2 domains $\leftarrow \Delta V/V$
▷ Update geometry of A_1 & A_2
31: Reset strains and stresses
32: $i \leftarrow i + 1$ ▷ Update counter i
33: $\alpha \leftarrow -g_s^{-1} i + \alpha_0$ ▷ Update α
34: **end while**

Afterward, the mesh gets prepared to perform a mechanical FEA: The material properties, E and ν, are assigned to elements that belong to bodies, conversely, E_c and ν_c to the elements of the capsule (line 9 - line 10). The force **F** and the boundary conditions are applied. From the FEA, the σ_{hyd} and σ_{vm} distributions are obtained (line 12); and the maximums identified (line 13-line 14).

An elemental scan is performed. For each element of the bodies A_1 and A_2, the stresses get normalized by the $\sigma_{\text{hyd}}^{\max}$ and $\sigma_{\text{vm}}^{\max}$ (line 16 - line 17). Depending on the location of the elements, a value of β is assigned: If it is located within the λl distance, then $\beta_j = 1$, else $\beta_j = 0$ (line 22).

Additionally, the elemental G_{f_j} is calculated following eq. (1). It considers the value of the elemental normalized von Mises stress, $\bar{\sigma}_{vm_j}$; if it was over $\bar{\sigma}_{\text{lim}}$, then $G_{f_j} = 0$, else, if the elemental normalized hydrostatic stress, $\bar{\sigma}_{hyd_j}$, is 0 or negative, then $G_{f_j} = \beta \bar{\sigma}_{hyd_j}$ (line 20 - line 24).

As mentioned in section 3.2, growth can be modeled as a thermal expansion (as also done in **(author?)** [52]). Therefore, the model gets prepared for a thermal expansion FEA on the bodies A_1 and A_2: G_f is given as temperature, and the reference temperature is taken as 0°; α is given as the expansion coefficient of the material. From the thermal FEA, the changes in volume are calculated, and with it, the new stress-free geometries of the bodies A_1 and A_2 are updated (line 30). The loop finishes with an update of the growth step i and the parameter α (line 33).

As a remark, the value of α was assumed to evolve linearly (the function $s(i)$ is a linear function with negative slope), from α_0 to 0 in a number of steps g_s (eq. (5)). It should be recalled that it is possible to have the same outcome with two different functions $s(i)$ as long as their integrals are the same. The larger the number of steps, the more stable and smooth the growth, although, the computational time increases.

$$\alpha_i = -\frac{1}{g_s} i + \alpha_0 \tag{5}$$

3.6. Parametric study

A response surface (*RS*) methodology was followed to explore the space of parameters of the bio-inspired process and to tune them.

3.6.1. Monitored variable:

A contact FEA of the problem described in section 3.1 is performed on the geometry at each growth step i of the bio-inspired algorithm. The evolution of the maximum von Mises' stress is monitored and evaluated as a percentage of the maximum von Mises' stress of the initial geometry. This stress was considered since it is a metric directly related to the maximum contact pressure, they are proportional to each other; moreover, the von Mises' criterion is also used to determine some failure inceptions in contact mechanics of ductile materials [54].

The number of growth steps for each run of the *RS* design was set manually to 20, small enough so that the computational time is not high, but large enough so that the growth is stable. With the *RS* it is possible to find the optimal value of α_0 for $g_s = 20$. For more stable and smooth growth, the number of steps g_s may increase and α_0 changed so that the area under the function in eq. (5) must be the same as the one found with the *RS*.

The simulations were performed in a 64-bit i7 processor @ 2.7 GHz, 16 GB RAM, Ubuntu 18.04 operating system. Each simulation of $g_s = 20$ took approximately 20 minutes. All the meshes were developed in GMSH [55]. A convergence analysis allowed us to define a minimum mesh size of 16.67E-3 mm.

3.6.2. Factors of the response surface:

From the parameters mentioned in table 3, the Poisson's ratio of the capsule and that of the bodies, the 'epiphyses' length factor, and the capsule thickness factor were defined according to the following statements. The Poisson's ratio of the bodies, ν, was fixed at 0.3, the same as the original material; and for the capsule, since it is an incompressible material, ν_c was set at 0.49. The capsule thickness factor $\bar{d}$ was set as small as possible so that there was at least one

line of mesh's elements between the pieces. The 'epiphyses' length factor, λ, was established following Saint-Venant's principle so that the zone allowed to grow was as long enough that reaches the distance where the stresses become uniform. Then, any growth of the domain at this distance would be uniform across the transverse area.

The remaining parameters, $\bar{\sigma}_{\text{lim}}$, θ, and α_0 were considered to have a great influence on the outcome of the response. The parameters were normalized within -1 and 1 and represented by the factors X_i (X_1, X_2, and X_3, corresponding to the parameters $\bar{\sigma}_{\text{lim}}$, θ, and α_0 respectively) (table 4). The intervals of the parameters were defined based on the experience of the researchers. Via several iterations, it was established that the optimal values of each parameter are within the chosen intervals.

3.6.3. Response surface function:

A *RS* of the selected parameters is proposed: $\widehat{Y_{rs}} = f(\bar{\sigma}_{\text{lim}}, \theta, \alpha_0)$. Since the parameters' intervals are relatively close to the optimum region, the curvature offered by a second-order polynomial is appropriated as an approximation function for the response surface [56]. The mathematical model for the response is described in eq. (6).

$$\widehat{Y_{rs}} = b_0 + \sum_{j=1}^{n} b_j X_j + \sum_{j=1}^{n} b_{jj} X_j^2 + \sum_{k=1}^{n-1} \sum_{j=k+1}^{n} b_{kj} X_k X_j \tag{6}$$

being $\widehat{Y_{rs}}$ the approximated response; b_0 is the value of the *RS* when all factors are set at the level 0; b_j are the linear regression coefficients; b_{jj}, and b_{jl} are regression coefficients of double factor interactions; and n is the total number of factors ($n = 3$).

3.6.4. Experiment design:

The design matrix was chosen as a Box-Wilson Central Composite Design (central composite design) (fig. 4) since it is suitable for fitting a second-order *RS* [57]. Specifically, a face-centered composite design was selected due to its simplicity; it only requires 3 levels of each factor (-1, 0 and 1) (table 4), and for 3 parameters a total of 15 combinations of factors, *i.e.* runs, are needed (table 5).

Table 4: Factor ranges for the design of the response surface.

parameter (*factor*)	$X_i = -1$	$X_i = 0$	$X_i = 1$
ν (-)		0.3	
ν_c (-)		0.49	
$\bar{d}$ (-)		3.40e−3	
λ (-)		2.1	
$\bar{\sigma}_{\text{lim}}$ (X_1)	0.2	0.3	0.4
θ (X_2)	500	5250	10000
α_0 (X_3)	0.01	0.05	0.09

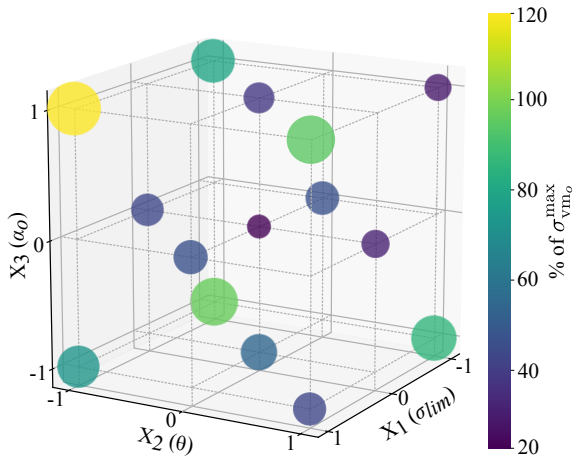

Figure 4: Bubble graphical representation of the outcome Y_c for all the computational runs. Each axis represents one normalized factor (X_1, X_2, and X_3). The size and color of each bubble represent the value of the outcome response Y_c.

4. Results

Table 5 shows the design matrix, the factors combination for each run c, the computational response Y_c, and regression coefficients b_j, b_{jj} and b_{kj}. In fig. 4 is shown a bubble graphical representation of the computational response for each run, which indicates that the minimum value of the response is within the ranges of the parameters.

Table 5: Response surface design matrix. Matrix of the face-centered composite design employed for the design of the *RS*, values of the computational measures, Y_c, and the obtained regression coefficients, b_j.

run	X_1	X_2	X_3	Y_c	*coefficients*	
1	−1	−1	−1	96.82%	b_0	2.53e−1
2	+1	−1	−1	73.19%	b_1	3.90e−2
3	−1	+1	−1	85.75%	b_2	−1.27e−1
4	+1	+1	−1	43.71%	b_3	8.04e−3
5	−1	−1	+1	79.91%	b_{12}	9.77e−3
6	+1	−1	+1	119.13%	b_{13}	2.12e−1
7	−1	+1	+1	29.35%	b_{23}	−4.29e−2
8	+1	+1	+1	94.79%	b_{11}	2.08e−1
9	−1	0	0	46.84%	b_{22}	1.14e−1
10	+1	0	0	46.85%	b_{33}	2.03e−1
11	0	−1	0	43.39%		
12	0	+1	0	31.52%		
13	0	0	−1	54.24%		
14	0	0	+1	38.58%		
15	0	0	0	22.61%		

The residual error e_c was estimated for each run through the arithmetic difference between the computational result, Y_c, and the estimated response, $\widehat{Y_{rs}}(X_1^c, X_2^c, X_3^c)$ (eq. (7)). The number of coefficients can be brought down by evaluating the standard deviation, σ_e, of the error e (eq. (8)); where N_e is the number of runs, N_f is the number of factors, and e_c is the error for each run. Then, the insignificant coefficients were identified with a Student's statistical test (t-test) and gradually removed until the standard deviation begins to augment; fig. 5 shows the evolution of σ_e.

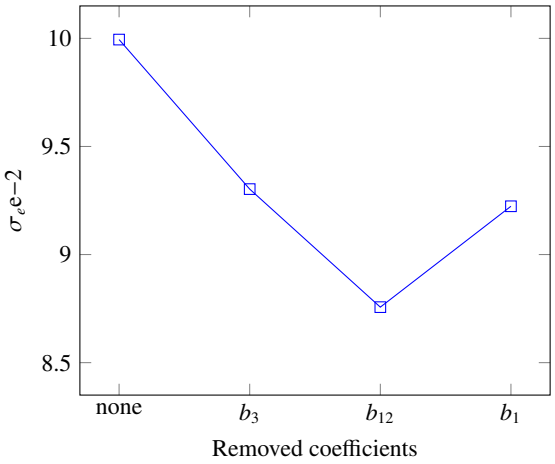

Figure 5: T-test performed to the coefficients of the response surface. The standard deviation of the error reduces as the coefficients b_3 and b_{12} are gradually removed, however, it increases when removing b_1.

The t-test shows that the linear coefficient of the factor X_3, b_3, and the double factor interaction coefficient, b_{12}, were statistically insignificant, therefore from now on they are set to 0 in 6. The second-order response surface with the coefficients after significance check is shown in section 4.

$$e_c = Y_c - \widehat{Y_{rs}}(X_1^c, X_2^c, X_3^c) \tag{7}$$

$$\sigma_e = \sqrt{\frac{1}{N_e - N_f} \sum_{j=1}^{N_e} e_c^2} \tag{8}$$

$$\begin{aligned} \widehat{Y_{rs}} \quad &= 0.2534 + 0.0390X_1 - 0.1273X_2 \\ &+0.2128X_1X_3 - 0.0429X_2X_3 \\ &+0.2082X_1X_1 + 0.1144X_2X_2 \\ &+0.2039X_3X_3 \end{aligned} \tag{9}$$

4.1. Optimization of the response surface factors

The response surface (section 4) can be optimized through the minimization shown in section 4.1, which will give the values of the factors X_1, X_2, and X_3.

$$\begin{aligned} &\min_{X_i} \quad \widehat{Y_{rs}} \\ &s.t. \quad -1 \leq X_i \leq 1 \qquad for \quad i = 1, 2, 3 \end{aligned} \tag{10}$$

The optimized value of $Yopt = 21.28\%$ was obtained with the following values of the factors: $X_{1^{opt}} = -0.1706$ ($\bar{\sigma}_{\text{lim}} = 0.2829$), $X_{2^{opt}} = 0.5849$ ($\theta = 8028.0646$) and $X_{3_{opt}} = 0.1506$ ($\alpha_0 = 0.0560$). The confidence interval of the response surface $U(\widehat{Y_{rs}})$ was estimated through section 4.1, for a confidence of 95%. The $var(\widehat{Y_{rs}})$ was calculated considering the covariant matrix of the coefficients $\mathbf{Cov(B)}$, and the jacobian of the model (the jacobian is shown in section 4.1). The uncertainty for the optimal solution is then $U(Y_{opt}) = \pm 4.9572\%$. A graphical representation of the second-order RS is shown in fig. 6. The surfaces are shown per pair of factors, the remaining factor i was set at the optimum value (X_i^{opt}). The outcome of each run is shown as black dots, the optimum value is shown in green.

$$U(\widehat{Y_{rs}}) = 2\sqrt{var(\widehat{Y_{rs}})} \tag{11}$$

$$var(\widehat{Y_{rs}}) = \mathbf{JCov(B)J}^T \tag{12}$$

$$\mathbf{J} = [X_1\ X_2\ X_{13}\ X_{23}\ X_1^2\ X_2^2\ X_3^2] \tag{13}$$

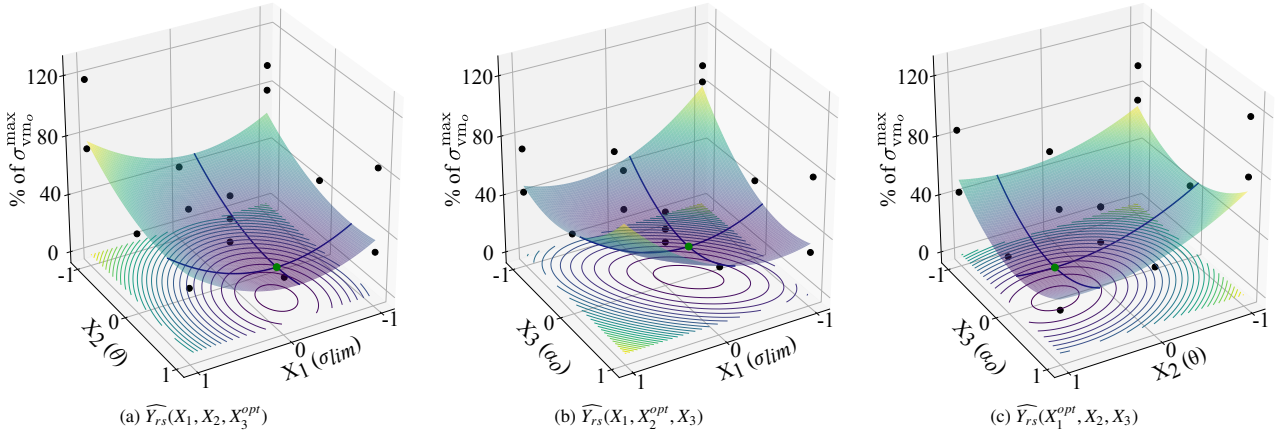

(a) $\widehat{Y_{rs}}(X_1, X_2, X_3^{opt})$ (b) $\widehat{Y_{rs}}(X_1, X_2^{opt}, X_3)$ (c) $\widehat{Y_{rs}}(X_1^{opt}, X_2, X_3)$

Figure 6: Diagram of the response surface. The graphic is divided into three surfaces in which the RS is calculated by pairing the factors X_1, X_2 and X_3, the remaining factor i was set at the optimum value (X_i^{opt}). The outcome of each run, Y_c, are shown as black dots, and the optimum is in green.

For the contact problem described in section 3.1, a new simulation of the bio-inspired algorithm was implemented setting the parameters at the values of the optimal response. The number of growth steps, g_s, was set at 20. After running the simulation, the maximum von Mises' stress of the last geometry was 25.8% of the initial; which is within the boundaries of the predicted value in section 4.1, $Y_{opt} \pm U(Y_{opt})$.

In fig. 7, the evolution of the von Mises' stress as a percentage of the one in the initial geometry, % of $\sigma_0^{\max}$, is shown at each step, as well as the profiles presented for each of the bodies at the initial, 6th, 12th, and 20th growth steps. The upper body is green-colored, whereas the lower one is reddish.

It should be pointed out that the algorithm appended material around the contact zones, increasing the area of contact, therefore reducing stress levels (fig. 7). The profiles were subjected to a smoothing process, as with other

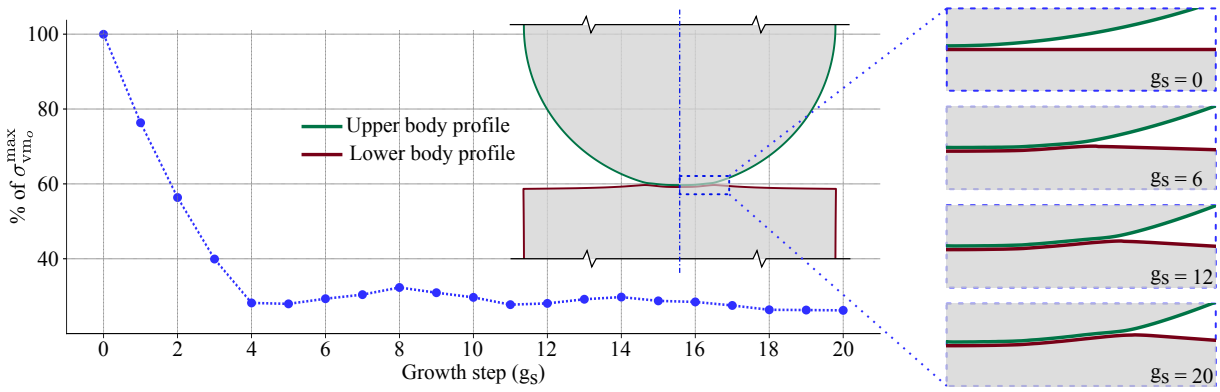

Figure 7: Evolution of the monitored variable. The evolution of the von Mises' stress as a percentage of the one in the initial geometry is shown at each step, and a scheme of the geometries at the 6th, 12th, and 20 steps are contrasted with the initial ($g_s = 0$). The upper body's profile is shown in green, conversely, the lower body's profile is shown in red.

generative tools, to diminish the effect of the discretized time and spatial growth. The smoothing was performed with 500 growth steps (α_0 is scaled accordingly), and to each final profile, a 3rd order function was fitted (one for the upper and one for the lower body) to obtain smooth profiles.

In fig. 8 the obtained stresses are compared. The von Mises' (fig. 8a) and hydrostatic stress (fig. 8b) distributions are compared at the initial (fig. 8-i), last geometry after 20 steps (fig. 8-ii), and after the smoothing process (fig. 8-iii). The von Mises' stress was reduced to 25.8% of the initial geometry in the 20-step profile and 16.1% in the smoothed profile, still within the boundaries of the predicted value ($Y_{opt} \pm U(Y_{opt})$). Similarly, the hydrostatic stress was reduced to 27.9% of the one in the initial geometry in the 20-step profile, and to 15.5% in the smoothed profile.

The optimized profiles of the upper and lower bodies are shown in fig. 9 and compared with the initial geometry. The upper body's final profile morphed in such a way that its radius increased when compared with the initial one (fig. 9a). The lower body's profile shows greater changes, it adapted quickly to the profile of the upper body increasing the contact area between them (fig. 9b).

The similarity between the profiles was evaluated through a *euclidean distance-based similarity score*. The score considers the distance between the two objects and goes from zero to one, the closer to 1, the more similar the objects. To determine the similarity between the curves, they were first aligned considering their lower vertical value. The distance between them is calculated as shown in section 4.1, and the similarity score as in section 4.1. Based on this score, the profiles show a great similarity at small radial distances fig. 9c.

$$d(p_1, p_2) = \sqrt{(x_{p_1} - x_{p_2})^2 + (y_{p_1} - y_{p_2})^2} \tag{14}$$

$$Sim(p_1, p_2) = \frac{1}{1 + d(p_1, p_2)} \tag{15}$$

The changes in the contact pressure profile from the initial and the morphed geometry (smoothed) are shown in

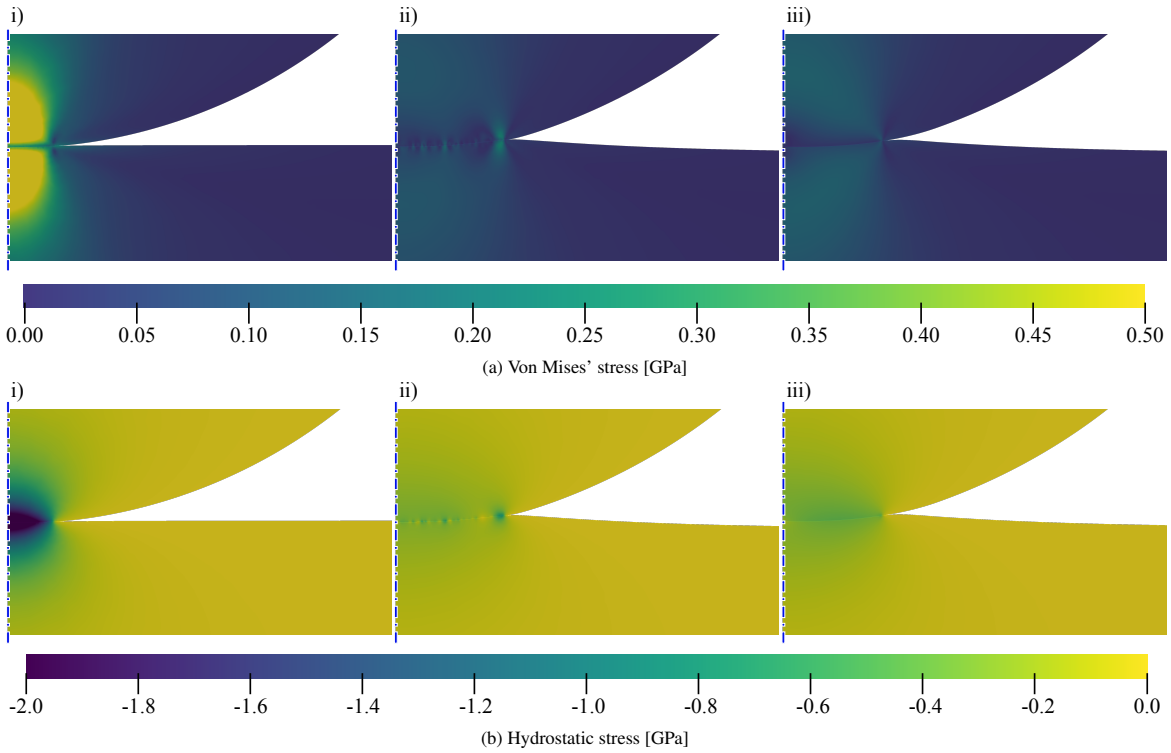

Figure 8: Stress distributions. Initial geometry (i), 20-steps (ii), after smoothing (iii).

fig. 9d. The pressure tends to become more uniform, and the maximum contact pressure is reduced to a 15% of the one in the initial geometry. This reduction in the overall contact pressure is related to the fact that the geometries of the contacting surfaces are more conformal between them, as in synovial joints. Moreover, the obtained profile shows the lower contact pressure at the center of the profile (at a radial distance of 0.0mm).

5. Discussion

A computational tool for surface shaping in unilateral contact problems inspired by the morphogenesis of synovial joints is presented in this work. The algorithm behind mimics the laws of cartilage growth (regulated by the mechanical environment). Its outcome was characterized by a parametric study. 7 dimensionless and normalized parameters were defined, from which 3 were identified as more influential in the outcome of the algorithm: $\bar{\sigma}_{\text{lim}}$, the normalized von Mises' stress that regulates growth, θ, which relates the material properties of the incompressible capsule and the pieces, and α_0, which is the initial growth coefficient.

A DoE analysis was performed through the design of a *RS*, which allowed us to determine the behavior of the monitored variable (maximum von Mises' stress) as a function of the parameters. A second-order *RS* was obtained depending on the parameters $\bar{\sigma}_{\text{lim}}$, θ and α_0. This response surface is valid within a normalized domain of the parameters (table 4). The coefficients of the *RS* indicate the relative influence of each parameter and their interactions on the outcome. The *RS* shows relatively high values of the second-order coefficients showing that there is a great

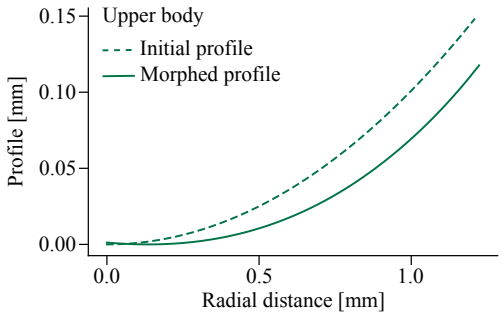

(a) Upper body profile changes

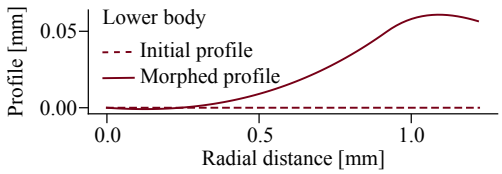

(b) Lower body profile changes

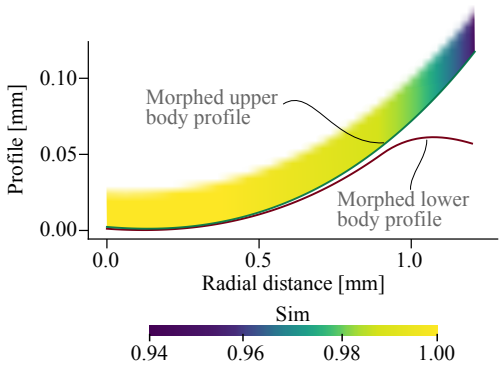

(c) Similarity score between the morphed upper and lower profiles

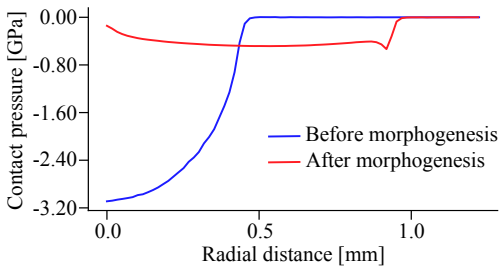

(d) Contact pressure before and after the morphogenesis

Figure 9: Contrasts among the profiles: Initial and final profiles. The upper and lower bodies' morphed profiles are compared with the initial ones, as well as the similarity score between the upper and lower morphed profiles in which the upper profile is color-mapped with the value of the similarity score. In these figures, the vertical axis is scaled 5 times the horizontal axis. Lastly, the contact pressure is shown before and after the morphogenesis.

interaction between the parameters, α_0 showed to have a large influence when interacting with the other two parameters, especially with $\bar{\sigma}_{\text{lim}}$. This shows that α_0 depends on the chosen value for σ_{lim} and θ. Moreover, since the linear coefficient of the parameter θ is relatively high (and negative), very small values of said parameter tend to increase

the monitored variable, whereas large values offer a better outcome. Conversely, its square coefficient, also large and positive contributes to finding a minimum of the response function within the normalized domain of parameters.

It was found that the response surface had a minimum within the valid domain. Hence, an optimization of the function was performed to find the values of $\bar{\sigma}_{\text{lim}}$, θ, and α_0 that offer the smallest value of the monitored variable. Then, a run of the algorithm with the parameters set at the optimum level with the same number of growth steps (20) used in the design of the *RS* was done. However, due to the nature of the method and the discretized growth of the domain (both in time and space), a non-smooth stress distribution was found due to the geometry obtained profiles. This effect was reduced by implementing a smooth transition between the on/off states given by $\bar{\sigma}_{\text{lim}}$ combined with an increment in growth steps (500); α_0 was diminished proportionally. Moreover, 3rd-order functions were fitted to the profiles to obtain a smooth geometry for stress analyses.

A profile of the surface was obtained for each of the pieces in contact. These profiles were obtained thanks to the slow growth of the domain during a given number of steps. The algorithm does small adjustments to the profile by adding gradually small portions of the material. The automatic shaping of the pieces followed a set of rules adopted from the cartilage growth process. The algorithm gradually increased the contact area between the bodies which ultimately translated to a reduction in the contact pressure as well as in the overall stresses. Interestingly, the obtained profiles had very close shapes for intermediate radial distances, as shown by the similarity score. Conversely, for very small distances the profiles seem to go smoothly in opposite ways, reducing slowly the contact pressure. The same occurs for large radial distances, but not as smooth as for small radiuses, which generate small pressure concentrator effects, nevertheless, the peak pressures are a lot smaller than in the initial geometry.

The obtained profiles can be scaled for any other similar contact problem by applying Buckingham's Pi Theorem. In general, the unilateral contact problem has 5 parameters, including the equivalent Young's modulus E^*, the magnitude of the applied force F, Poisson's ratio of the pieces $\nu_{1,2}$, and the width of the pieces l (the radiuses are not considered since they are a function of the width of the pieces). The theorem reduces the problem to 3 dimensionless numbers: $\nu_{1,2}$ and a number $\Phi = F/(l^2E^*)$; for same materials in contact $\Phi = (2F(1-\nu^2))/(l^2E)$. The dimensionless number Φ can then be used as a scale factor to obtain the profile for a given set of F, and materials in contact ($E_{1,2}$ and $\nu_{1,2}$). The structure of this scale factor is similar to the ones found in the literature to scale the logarithmic contact surface proposed by Lundberg [58].

Other authors have performed shape optimization for contacting surfaces, in which they define a cost function and aim to minimize it [15, 16, 14]. However, in those works, only the shape of one of the contacting surfaces is optimized in the attempt of achieving a uniform contact pressure. Recently, in a work developed by **(author?)** [27], a combination of the interface shape and the material stiffness optimization to obtain a uniform contact stress distribution was done. They focused just on the contact interface and changed its shape equally for both surfaces in contact. Conversely, in this paper, we found the profiles of the upper and lower bodies similar for small radial distances.

The work presented here shows that by applying the basic laws of cartilage tissue adaptation to mechanical loading

an efficient profile can be achieved. In this new profile, the stresses are reduced as well as the contact pressure. Hence, this work corroborates that nature distributes wisely the material within a domain so that the stress gets distributed as uniformly as possible, contributing to a large lifespan of the joints.

The algorithm implemented here can be improved by including other biological processes in parallel with the shaping of the contact surface, such as changes in the local material stiffness (during the ossification the tissue changes its material properties gradually until fully ossified, adapting to the mechanical loading). Nevertheless, should be considered the computational cost that this implies and the increase in the number of parameters of the algorithm to be tuned. Moreover, an analysis of the influence of the type of function used for the growth coefficient α should be performed in future works, as well as a way to make the growth less dependent on temporal and space discretization, perhaps with a parametric curve mapping. Additionally, it should be considered that the DoE method with the design of the *RS* does not assure the finding of a global optimum, since it is highly dependent on the ranges of the parameters. Furthermore, experimental validations would be desirable to evaluate the manufacturing feasibility of the generated profiles and the real performance in terms of contact load distribution.

6. Conclusions

Currently, mechanical joint design has not been approached by mimicking nature's joint morphogenesis process. Based on this process, this work proposes an algorithm for the design of pieces in contact. The algorithm was implemented in a FEM framework and the feasibility of obtaining an adapted joint surface was evaluated. The more influential parameters of the bio-inspired process were identified and optimized through a response surface. The results show that the algorithm, by mimicking the cartilage growth rules, adapts the geometry of the joint contact surfaces in such a way that the contact stresses are distributed uniformly. Since the proposed bio-inspired algorithm was implemented in a dimensionless fashion, the found solution for the contact profiles can be used for similar problems. This work demonstrates that nature's laws for joint morphogenesis can be adapted for the generative design of contact surfaces of mechanical joints. The latter opens the possibility to further develop the algorithm to address more complex settings (combined loading, non-linear materials, dynamic setups, etc). This contribution is a step forward in the scope of bio-inspired generative design.

Acknowledgements

This research was supported by French Research National Agency (ANR) Grant No. ANR-20-CE10-0008.

References

[1] M. Gralow, F. Weigand, D. Herzog, T. Wischeropp, C. Emmelmann, Biomimetic design and laser additive manufacturing—A perfect symbiosis?, Journal of Laser Applications 32 (2) (2020) 021201. doi:10.2351/1.5131642.

[2] E. Picault, E. Mermoz, T. Thouveny, J. M. Linares, Smart pressure distribution estimation in biological joints for mechanical bio-inspired design, CIRP Annals 67 (1) (2018) 153–156. doi:10.1016/j.cirp.2018.04.116.
URL https://doi.org/10.1016/j.cirp.2018.04.116

[3] A. Borsari, Human mimicry and imitation: The case of biomimetics, Aisthesis (Italy) 10 (1) (2017) 51–61. doi:10.13128/Aisthesis-20903.

[4] R. Vertechy, V. Parenti-Castelli, C. Menon, Biologically Inspired Joints for Innovative Articulations Concepts, Tech. rep., University of Bologna - DIEM ESA, Bologna, Italy (2005).

[5] R. van der Linde, J. Caarls, C. Menon, J. Verhoef, Biological Inspired Joints for Innovative Articulation Concepts, Tech. rep., TUDelft, ESA (2006).

[6] D. Sysaykeo, J. M. Linares, E. Mermoz, Wear Behavior of a Bio-inspired Bearing for off-center Loads, Journal of Bionic Engineering 17 (6) (2020) 1251–1262. doi:10.1007/s42235-020-0107-3.

[7] D. Sysaykeo, E. Mermoz, T. Thouveny, Clearance and design optimization of bio-inspired bearings under off-center load, CIRP Annals 69 (1) (2020) 121–124. doi:10.1016/j.cirp.2020.03.006.

[8] A. Sanz-Idirin, S. Arroyave-Tobon, J.-M. Linares, P. J. Arrazola, Load bearing performance of mechanical joints inspired by elbow of quadrupedal mammals, Bioinspiration & Biomimetics 16 (4) (2021) 046025. doi:10.1088/1748-3190/abeb57.

[9] M. Pacifici, E. Koyama, M. Iwamoto, Mechanisms of synovial joint and articular cartilage formation: Recent advances, but many lingering mysteries, Birth Defects Research Part C - Embryo Today: Reviews 75 (3) (2005) 237–248. doi:10.1002/bdrc.20050.

[10] A. F. Carrera-Pinzón, K. Márquez-Flórez, R. H. Kraft, S. Ramtani, D. A. Garzón-Alvarado, Computational model of a synovial joint morphogenesis, Biomechanics and Modeling in Mechanobiology 19 (5) (2020) 1389–1402. doi:10.1007/s10237-019-01277-4.

[11] J. Henderson, D. Carter, Mechanical induction in limb morphogenesis: the role of growth-generated strains and pressures, Bone 31 (6) (2002) 645–653. doi:10.1016/S8756-3282(02)00911-0.

[12] P. Aghajanian, S. Mohan, The art of building bone: Emerging role of chondrocyte-to-osteoblast transdifferentiation in endochondral ossification, Bone Research 6 (1). doi:10.1038/s41413-018-0021-z.

[13] A. Klarbring, J. Haslinger, On almost constant contact stress distributions by shape optimization, Structural Optimization 5 (4) (1993) 213–216. doi:10.1007/BF01743581.

[14] E. A. Fancello, R. A. Feijóo, Shape optimization in frictionless contact problems, International Journal for Numerical Methods in Engineering 37 (13) (1994) 2311–2335. doi:10.1002/nme.1620371310.
URL https://onlinelibrary.wiley.com/doi/10.1002/nme.1620371310

[15] W. Li, Q. Li, G. P. Steven, Y. Xie, An evolutionary shape optimization for elastic contact problems subject to multiple load cases, Computer Methods in Applied Mechanics and Engineering 194 (30-33) (2005) 3394–3415. doi:10.1016/j.cma.2004.12.024.
URL www.elsevier.com/locate/cmahttps://linkinghub.elsevier.com/retrieve/pii/S0045782505000538

[16] W. Li, Q. Li, G. P. Steven, Y. M. Xie, An evolutionary shape optimization procedure for contact problems in mechanical designs, Proceedings of the Institution of Mechanical Engineers, Part C: Journal of Mechanical Engineering Science 217 (4) (2003) 435–446. doi:10.1243/095440603321509711.
URL https://journals-sagepub-com.lama.univ-amu.fr/doi/abs/10.1243/09544060332150971 1http://journals.sagepub.com/doi/10.1243/095440603321509711

[17] D. Hilding, A. Klarbring, J. Petersson, Optimization of Structures in Unilateral Contact, Applied Mechanics Reviews 52 (4) (1999) 139–160. doi:10.1115/1.3098931.

[18] N. L. Pedersen, On optimization of interference fit assembly, Structural and Multidisciplinary Optimization 54 (2) (2016) 349–359. doi:10.1007/s00158-016-1419-0.

[19] H. Ou, B. Lu, Z. S. Cui, C. Lin, A direct shape optimization approach for contact problems with boundary stress concentration, Journal of Mechanical Science and Technology 27 (9) (2013) 2751–2759. doi:10.1007/s12206-013-0721-7.
URL www.springerlink.com/content/1738-494xhttp://link.springer.com/10.1007/s12206-013-0721-7

[20] H. Kristiansen, K. Poulios, N. Aage, Topology optimization for compliance and contact pressure distribution in structural problems with friction, Computer Methods in Applied Mechanics and Engineering 364 (2020) 112915. doi:https://doi.org/10.1016/j.cma.2020.112915.
URL https://www.sciencedirect.com/science/article/pii/S0045782520300980

[21] Y. Tada, S. Nishihara, Optimum shape design of contact surface with finite element method, Advances in Engineering Software 18 (2) (1993) 75–85. doi:10.1016/0965-9978(94)90001-9.
URL https://linkinghub.elsevier.com/retrieve/pii/0965997894900019

[22] R. L. Benedict, Maximum stiffness design for elastic bodies in contact, Journal of Mechanical Design, Transactions of the ASME 104 (4) (1982) 825–830. doi:10.1115/1.3256443.

[23] N. Strömberg, A. Klarbring, Topology optimization of structures in unilateral contact, Structural and Multidisciplinary Optimization 41 (1) (2010) 57–64. doi:10.1007/s00158-009-0407-z.

[24] Q. Lin, Y. Zhou, N. Yang, J. Hong, C. Wang, Design of component structure in assemblies for simultaneously regulating contact pressure distribution and natural frequencies, European Journal of Mechanics, A/Solids 94 (28) (2022) 104557. doi:10.1016/j.euromechsol.2022.104557.

[25] A. Myslinski, Piecewise constant level set method for topology optimization of unilateral contact problems, Advances in Engineering Software 80 (C) (2015) 25–32. doi:10.1016/j.advengsoft.2014.09.020.

[26] M. Lawry, K. Maute, Level set shape and topology optimization of finite strain bilateral contact problems, International Journal for Numerical Methods in Engineering 113 (8) (2018) 1340–1369. arXiv:1701.06092, doi:10.1002/nme.5582.

[27] Y. Zhou, Q. Lin, J. Hong, N. Yang, Combined interface shape and material stiffness optimization for uniform distribution of contact stress, Mechanics Based Design of Structures and Machines 0 (0) (2020) 1–15. doi:10.1080/15397734.2020.1860086.
URL https://doi.org/10.1080/15397734.2020.1860086

[28] S. Arroyave-Tobon, K. Marquez-Florez, P. Heymann, J.-M. Linares, Generative design of joint contact surfaces inspired by biological morphogenesis, CIRP Annals 00 (2022) 4–7. doi:10.1016/j.cirp.2022.04.006.
URL https://doi.org/10.1016/j.cirp.2022.04.006

[29] D. Rux, R. S. Decker, E. Koyama, M. Pacifici, Joints in the appendicular skeleton: Developmental mechanisms and evolutionary influences., Current topics in developmental biology 133 (2019) 119–151. doi:10.1016/bs.ctdb.2018.11.002.
URL https://linkinghub.elsevier.com/retrieve/pii/S0070215318300814http://www.ncbi.nlm.nih.gov/pubmed/30902250http://www.pubmedcentral.nih.gov/articlerender.fcgi?artid=PMC6988388https://www.sciencedirect.com/science/article/pii/S0070215318300814

[30] K. M. Márquez-Flórez, J. R. Monaghan, S. J. Shefelbine, A. Ramirez-Martínez, D. A. Garzón-Alvarado, A computational model for the joint onset and development, Journal of Theoretical Biology 454 (2018) 345–356. doi:10.1016/j.jtbi.2018.04.015.

[31] E. Koyama, Y. Shibukawa, M. Nagayama, H. Sugito, B. Young, T. Yuasa, T. Okabe, T. Ochiai, N. Kamiya, R. B. Rountree, D. M. Kingsley, M. Iwamoto, M. Enomoto-Iwamoto, M. Pacifici, A distinct cohort of progenitor cells participates in synovial joint and articular cartilage formation during mouse limb skeletogenesis, Developmental Biology 316 (1) (2008) 62–73. arXiv:NIHMS150003, doi:10.1016/j.ydbio.2008.01.012.

[32] A. M. Nalin, T. K. Greenlee, L. J. Sandell, Collagen gene expression during development of avian synovial joints: transient expression of types II and XI collagen genes in the joint capsule., Developmental dynamics : an official publication of the American Association of Anatomists 203 (3) (1995) 352–362. doi:10.1002/aja.1002030307.

[33] S. Kimura, K. Shiota, Sequential changes of programmed cell death in developing fetal mouse limbs and its possible roles in limb morphogenesis, Journal of Morphology 229 (3) (1996) 337–346. doi:10.1002/(SICI)1097-4687(199609)229:3<337::AID-JMOR8>3.0.CO;2-V.

[34] K. A. Roddy, N. C. Nowlan, P. J. Prendergast, P. Murphy, 3D representation of the developing chick knee joint: a novel approach integrating multiple components., Journal of anatomy 214 (3) (2009) 374–87. doi:10.1111/j.1469-7580.2008.01040.x.

[35] N. C. Nowlan, J. Sharpe, Joint shape morphogenesis precedes cavitation of the developing hip joint, Journal of Anatomy 224 (4) (2014) 482–489. doi:10.1111/joa.12143.

[36] N. C. Nowlan, Biomechanics of foetal movement, European Cells and Materials 29 (0) (2015) 1–21.

[37] A. S. Pollard, I. M. McGonnell, A. A. Pitsillides, Mechanoadaptation of developing limbs: shaking a leg, Journal of Anatomy 224 (6) (2014) 615–623. doi:10.1111/joa.12171.

[38] D. R. Carter, T. Orr, D. P. Fyhrie, D. J. Schurman, Influences of Mechanical Stress on Prenatal and Postnatal Skeletal Development, Clinical Orthopaedics and Related Research 219 (NA;) (1987) 237 – 250. doi:10.1097/00003086-198706000-00034.

[39] D. R. Carter, Mechanical loading history and skeletal biology, Journal of Biomechanics 20 (11-12) (1987) 1095–1109. doi:10.1016/0021-9290(87)90027-3.

[40] D. Carter, D. Fyrhrie, R. Whalen, T. Orr, D. Schurman, D. Rapperport, Control of chondro-osseous skeletal biology by mechanical energy, Journal of Biomechanics 20 (8) (1987) 815. doi:10.1016/0021-9290(87)90098-4.

[41] D. R. Carter, M. Wong, The role of mechanical loading histories in the development of diarthrodial joints, Journal of Orthopaedic Research 6 (6) (1988) 804–816. doi:10.1002/jor.1100060604.

[42] D. R. Carter, M. Wong, Mechanical stresses and endochondral ossification in the chondroepiphysis, Journal of Orthopaedic Research 6 (1) (1988) 148–154. doi:10.1002/jor.1100060120.

[43] X. Wang, J. Mao, Chondrocyte Proliferation of the Cranial Base Cartilage upon in vivo Mechanical Stresses, Journal of Dental Research 81 (10) (2002) 701–705. doi:10.1177/154405910208101009.

[44] X. Wang, J. J. Mao, Accelerated Chondrogenesis of the Rabbit Cranial Base Growth Plate by Oscillatory Mechanical Stimuli, Journal of Bone and Mineral Research 17 (10) (2002) 1843–1850. doi:10.1359/jbmr.2002.17.10.1843.

[45] M. Wong, M. Siegrist, K. Goodwin, Cyclic tensile strain and cyclic hydrostatic pressure differentially regulate expression of hypertrophic markers in primary chondrocytes, Bone 33 (4) (2003) 685–693. doi:10.1016/S8756-3282(03)00242-4.

[46] H. Othman, E. J. Thonar, J. J. Mao, Modulation of neonatal growth plate development by ex vivo intermittent mechanical stress, Journal of Biomechanics 40 (12) (2007) 2686–2693. doi:10.1016/j.jbiomech.2006.12.014.

[47] L. Bian, D. Y. Zhai, E. C. Zhang, R. L. Mauck, J. A. Burdick, Dynamic Compressive Loading Enhances Cartilage Matrix Synthesis and Distribution and Suppresses Hypertrophy in hMSC-Laden Hyaluronic Acid Hydrogels, Tissue Engineering Part A 18 (7-8) (2012) 715–724. doi:10.1089/ten.tea.2011.0455.

[48] C. C. van Donkelaar, R. Huiskes, The PTHrP–Ihh Feedback Loop in the Embryonic Growth Plate Allows PTHrP to Control Hypertrophy and Ihh to Regulate Proliferation, Biomechanics and Modeling in Mechanobiology 6 (1-2) (2007) 55–62. doi:10.1007/s10237-006-0035-0.

[49] E. Koyama, T. Ochiai, R. B. Rountree, D. M. Kingsley, M. Enomoto-Iwamoto, M. Iwamoto, M. Pacifici, Synovial Joint Formation during Mouse Limb Skeletogenesis: Roles of Indian Hedgehog Signaling, Annals of the New York Academy of Sciences 1116 (1) (2007) 100–112. doi:10.1196/annals.1402.063.

[50] F. Long, D. M. Ornitz, Development of the Endochondral Skeleton, Cold Spring Harbor Perspectives in Biology 5 (1) (2013) a008334–a008334. doi:10.1101/cshperspect.a008334.

[51] J. H. Heegaard, G. S. Beaupré, D. R. Carter, G. S. Beaupre, D. R. Carter, Mechanically modulated cartilage growth may regulate joint surface morphogenesis, Journal of Orthopaedic Research 17 (4) (1999) 509–517. doi:10.1002/jor.1100170408.

[52] M. Giorgi, A. Carriero, S. J. Shefelbine, N. C. Nowlan, Mechanobiological simulations of prenatal joint morphogenesis., Journal of biomechanics 47 (5) (2014) 989–95. doi:10.1016/j.jbiomech.2014.01.002.

[53] I. Villemure, I. A. Stokes, Growth plate mechanics and mechanobiology. A survey of present understanding, Journal of Biomechanics 42 (12) (2009) 1793–1803. doi:10.1016/j.jbiomech.2009.05.021.

[54] V. Brizmer, Y. Kligerman, I. Etsion, The effect of contact conditions and material properties on the elasticity terminus of a spherical contact, International Journal of Solids and Structures 43 (18-19) (2006) 5736–5749. doi:10.1016/j.ijsolstr.2005.07.034.

[55] C. Geuzaine, J. F. Remacle, Gmsh: A 3-D finite element mesh generator with built-in pre- and post-processing facilities, International Journal for Numerical Methods in Engineering 79 (11) (2009) 1309–1331. doi:10.1002/nme.2579.

[56] D. C. A. S. U. Montgomery, D esign and Analysis of Experiments Ninth Edition, 2017.
URL www.wiley.com/go/permissions.%0Ahttps://lccn.loc.gov/2017002355

[57] G. E. P. Box, K. B. Wilson, On the Experimental Attainment of Optimum Conditions, Journal of the Royal Statistical Society: Series B (Methodological) 13 (1) (1951) 1–38. doi:10.1111/j.2517-6161.1951.tb00067.x.

[58] P. Johns, R. Gohar, Roller bearings under radial and eccentric loads, Tribology International 14 (3) (1981) 131–136. doi:10.1016/0301-679X(81)90058-X.
URL https://linkinghub.elsevier.com/retrieve/pii/0301679X8190058X